PHYSICAL REVIEW LETTERS **128,** 252002 (2022)

Deeply Virtual Compton Scattering Cross Section at High Bjorken x_B

F. Georges,[1] M. N. H. Rashad,[2] A. Stefanko,[3] M. Dlamini,[4] B. Karki,[4] S. F. Ali,[5] P-J. Lin,[1] H-S Ko,[1,6] N. Israel,[4]
D. Adikaram,[7] Z. Ahmed,[8] H. Albataineh,[9] B. Aljawrneh,[10] K. Allada,[11] S. Allison,[2] S. Alsalmi,[12] D. Androic,[13] K. Aniol,[14]
J. Annand,[15] H. Atac,[16] T. Averett,[17] C. Ayerbe Gayoso,[17] X. Bai,[18] J. Bane,[19] S. Barcus,[17] K. Bartlett,[17] V. Bellini,[20]
R. Beminiwattha,[21] J. Bericic,[7] D. Biswas,[22] E. Brash,[23] D. Bulumulla,[2] J. Campbell,[24] A. Camsonne,[7] M. Carmignotto,[5]
J. Castellano,[25] C. Chen,[22] J-P. Chen,[7] T. Chetry,[4] M. E. Christy,[22] E. Cisbani,[26] B. Clary,[27] E. Cohen,[28] N. Compton,[4]
J. C. Cornejo,[17,3] S. Covrig Dusa,[7] B. Crowe,[29] S. Danagoulian,[10] T. Danley,[4] F. De Persio,[26] W. Deconinck,[17]
M. Defurne,[30] C. Desnault,[1] D. Di,[18] M. Duer,[28] B. Duran,[16] R. Ent,[7] C. Fanelli,[11] G. Franklin,[3] E. Fuchey,[27] C. Gal,[18]
D. Gaskell,[7] T. Gautam,[22] O. Glamazdin,[31] K. Gnanvo,[18] V. M. Gray,[17] C. Gu,[18] T. Hague,[12] G. Hamad,[4] D. Hamilton,[15]
K. Hamilton,[15] O. Hansen,[7] F. Hauenstein,[2] W. Henry,[16] D. W. Higinbotham,[7] T. Holmstrom,[32] T. Horn,[5,7] Y. Huang,[18]
G. M. Huber,[8] C. E. Hyde,[2] H. Ibrahim,[33] C-M. Jen,[34] K. Jin,[18] M. Jones,[7] A. Kabir,[12] C. Keppel,[7] V. Khachatryan,[7,35,36]
P. M. King,[4] S. Li,[37] W. B. Li,[8] J. Liu,[18] H. Liu,[38] A. Liyanage,[22] J. Magee,[17] S. Malace,[7] J. Mammei,[39] P. Markowitz,[25]
E. McClellan,[7] M. Mazouz,[40] F. Meddi,[26] D. Meekins,[7] K. Mesik,[41] R. Michaels,[7] A. Mkrtchyan,[5] R. Montgomery,[15]
C. Muñoz Camacho,[1,*] L. S. Myers,[7] P. Nadel-Turonski,[7] S. J. Nazeer,[22] V. Nelyubin,[18] D. Nguyen,[18] N. Nuruzzaman,[22]
M. Nycz,[12] O. F. Obretch,[27] L. Ou,[11] C. Palatchi,[18] B. Pandey,[22] S. Park,[35] K. Park,[2] C. Peng,[42] R. Pomatsalyuk,[31]
E. Pooser,[7] A. J. R. Puckett,[27] V. Punjabi,[43] B. Quinn,[3] S. Rahman,[39] P. E. Reimer,[44] J. Roche,[4] I. Sapkota,[5] A. Sarty,[45]
B. Sawatzky,[7] N. H. Saylor,[46] B. Schmookler,[11] M. H. Shabestari,[47] A. Shahinyan,[48] S. Sirca,[49] G. R. Smith,[7]
S. Sooriyaarachchilage,[22] N. Sparveris,[16] R. Spies,[39] T. Su,[12] A. Subedi,[47] V. Sulkosky,[50] A. Sun,[3] L. Thorne,[3] Y. Tian,[51]
N. Ton,[18] F. Tortorici,[20] R. Trotta,[52] G. M. Urciuoli,[26] E. Voutier,[1] B. Waidyawansa,[7] Y. Wang,[17] B. Wojtsekhowski,[7]
S. Wood,[7] X. Yan,[53] L. Ye,[47] Z. Ye,[18] C. Yero,[25] J. Zhang,[18] Y. Zhao,[35] and P. Zhu[54]

(Jefferson Lab Hall A Collaboration)

[1]*Université Paris-Saclay, CNRS/IN2P3, IJCLab, 91405 Orsay, France*
[2]*Old Dominion University, Norfolk, Virginia 23529, USA*
[3]*Carnegie Mellon University, Pittsburgh, Pennsylvania 15213, USA*
[4]*Ohio University, Athens, Ohio 45701, USA*
[5]*Catholic University of America, Washington, DC 20064, USA*
[6]*Seoul National University, 1 Gwanak-ro, Gwanak-gu, 08826 Seoul, Korea*
[7]*Thomas Jefferson National Accelerator Facility, Newport News, Virginia 23606, USA*
[8]*University of Regina, Regina, Saskatchewan, S4S 0A2 Canada*
[9]*Texas A&M University-Kingsville, Kingsville, Texas 78363, USA*
[10]*North Carolina Agricultural and Technical State University, Greensboro, North Carolina 27411, USA*
[11]*Massachusetts Institute of Technology, Cambridge, Massachusetts 02139, USA*
[12]*Kent State University, Kent, Ohio 44240, USA*
[13]*University of Zagreb, Trg Republike Hrvatske 14, 10000 Zagreb, Croatia*
[14]*California State University, Los Angeles, Los Angeles, California 90032, USA*
[15]*SUPA School of Physics and Astronomy, University of Glasgow, Glasgow G12 8QQ, United Kingdom*
[16]*Temple University, Philadelphia, Pennsylvania 19122, USA*
[17]*The College of William and Mary, Williamsburg, Virginia 23185, USA*
[18]*University of Virginia, Charlottesville, Virginia 22904, USA*
[19]*University of Tennessee, Knoxville, Tennessee 37996, USA*
[20]*Istituto Nazionale di Fisica Nucleare, Dipartimento di Fisica delle Università degli di Catania, I-95123 Catania, Italy*
[21]*Syracuse University, Syracuse, New York 13244, USA*
[22]*Hampton University, Hampton, Virginia 23669, USA*
[23]*Christopher Newport University, Newport News, Virginia 23606, USA*
[24]*Dalhousie University, Nova Scotia, NS B3H 4R2, Canada*
[25]*Florida International University, Miami, Florida 33199, USA*
[26]*Istituto Nazionale di Fisica Nucleare—Sezione di Roma, Piazzale Aldo Moro, 2—00185 Roma, Italy*
[27]*University of Connecticut, Storrs, Connecticut 06269, USA*
[28]*Tel Aviv University, Tel Aviv-Yafo 6997801, Israel*
[29]*North Carolina Central University, Durham, North Carolina 27707, USA*
[30]*CEA Saclay, 91191 Gif-sur-Yvette, France*

0031-9007/22/128(25)/252002(7)

Published by the American Physical Society

[31]*Kharkov Institute of Physics and Technology, Kharkov 61108, Ukraine*
[32]*Longwood University, Farmville, Virginia 23901, USA*
[33]*Cairo University, Cairo 121613, Egypt*
[34]*Virginia Polytechnic Institute & State University, Blacksburg, Virginia 234061, USA*
[35]*Stony Brook, State University of New York, New York 11794, USA*
[36]*Cornell University, Ithaca, New York 14853, USA*
[37]*University of New Hampshire, Durham, New Hampshire 03824, USA*
[38]*Columbia University, New York, New York 10027, USA*
[39]*University of Manitoba, Winnipeg, MB R3T 2N2, Canada*
[40]*Faculté des Sciences de Monastir, Monastir 5019, Tunisia*
[41]*Rutgers University, New Brunswick, New Jersey 08854, USA*
[42]*Duke University, Durham, North Carolina 27708, USA*
[43]*Norfolk State University, Norfolk, Virginia 23504, USA*
[44]*Physics Division, Argonne National Laboratory, Lemont, Illinois 60439, USA*
[45]*Saint Mary's University, Halifax, Nova Scotia B3H 3C3, Canada*
[46]*Rensselaer Polytechnic Institute, Troy, New York 12180, USA*
[47]*Mississippi State University, Mississippi State, Mississippi 39762, USA*
[48]*AANL, 2 Alikhanian Brothers Street, 0036 Yerevan, Armenia*
[49]*Faculty of Mathematics and Physics, University of Ljubljana, 1000 Ljubljana, Slovenia*
[50]*University of Virginia, Charlottesville, Virginia 22904, USA*
[51]*Shandong University, Jinan 250100, China*
[52]*Duquesne University, 600 Forbes Avenue, Pittsburgh, Pennsylvania 15282, USA*
[53]*Huangshan University, Tunxi, Daizhen Road 245041, China*
[54]*University of Science and Technology of China, Hefei, Anhui 230026, China*

(Received 4 December 2021; revised 28 March 2022; accepted 18 April 2022; published 23 June 2022)

We report high-precision measurements of the deeply virtual Compton scattering (DVCS) cross section at high values of the Bjorken variable x_B. DVCS is sensitive to the generalized parton distributions of the nucleon, which provide a three-dimensional description of its internal constituents. Using the exact analytic expression of the DVCS cross section for all possible polarization states of the initial and final electron and nucleon, and final state photon, we present the first experimental extraction of all four helicity-conserving Compton form factors (CFFs) of the nucleon as a function of x_B, while systematically including helicity flip amplitudes. In particular, the high accuracy of the present data demonstrates sensitivity to some very poorly known CFFs.

DOI: 10.1103/PhysRevLett.128.252002

In this Letter, we present an experimental determination of the four complex helicity-conserving amplitudes of the $\gamma^* p \to \gamma p$ amplitude, measured in the deeply virtual Compton scattering (DVCS) reaction $ep \to ep\gamma$. This amplitude is illustrated in Fig. 1, which also defines our kinematic nomenclature. The Bjorken limit of DVCS, first described in [1], is defined by large virtuality Q^2 and large invariant "energy" $\nu = q \cdot P/M$ of the virtual photon at fixed $x_B = Q^2/(2q \cdot P)$ and small net momentum transfer to the proton. QCD theorems [2,3] prove the DVCS amplitude factorizes into a hard perturbative kernel and a soft part described by light cone matrix elements [4] of quark and gluon operators. In this scaling limit, the $\gamma^* p \to \gamma p$ amplitude reduces to just four complex amplitudes, whose Q^2 dependence is determined by QCD evolution equations [5]. The light cone matrix elements, also called generalized parton distributions (GPDs), encode tomographic images

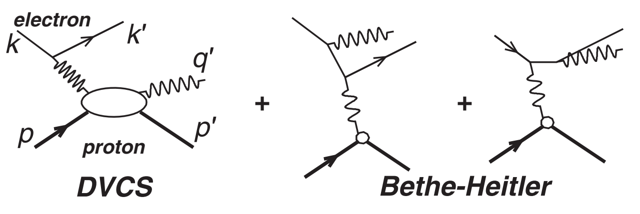

FIG. 1. Lowest-order QED diagrams for the process $ep \to ep\gamma$, including the DVCS and Bethe-Heitler (BH) amplitudes. The external momentum four vectors are defined on the diagram. The virtual photon momenta are $q = k - k'$ in the DVCS amplitudes and $\Delta = q - q'$ in the BH amplitudes. The invariants are $W^2 = (q + p)^2$, $Q^2 = -q^2 > 0$, $t = \Delta^2$, $x_B = Q^2/(2p \cdot q)$, and the DVCS scaling variable $\xi = -\bar{q}^2/(\bar{q} \cdot P) \approx x_B/(2 - x_B)$, with $\bar{q} = (q + q')/2$ and $P = p + p'$.

TABLE I. Main kinematic variables for each of the nine (Q^2, x_B) settings where the DVCS cross section is reported. E_b is the incident electron energy, E_γ and $-t_{\rm min}$ correspond to a final state photon emitted parallel to $\mathbf{q} = \mathbf{k} - \mathbf{k}'$ at the nominal Q^2, x_B values listed. For each setting, the cross section is measured as a function of t (3 to 5 bins depending on the setting) and in 24 bins in ϕ. The accumulated charge, corrected by the acquisition dead time, is listed in the row labeled $\int Qdt$. The last row of the table indicates the number of statistically independent measurements (bins) for each x_B setting, including helicity dependence.

Setting	Kin-36-1	Kin-36-2	Kin-36-3	Kin-48-1	Kin-48-2	Kin-48-3	Kin-48-4	Kin-60-1	Kin-60-3
x_B	0.36			0.48				0.60	
E_b (GeV)	7.38	8.52	10.59	4.49	8.85	8.85	10.99	8.52	10.59
Q^2 (GeV^2)	3.20	3.60	4.47	2.70	4.37	5.33	6.90	5.54	8.40
E_γ (GeV)	4.7	5.2	6.5	2.8	4.7	5.7	7.5	4.6	7.1
$-t_{\rm min}$ (GeV^2)	0.16	0.17	0.17	0.32	0.34	0.35	0.36	0.66	0.70
$\int Qdt$ (C)	1.2	1.7	1.3	2.2	2.2	3.7	5.7	6.4	18.5
Number of data bins	672			912				480	

correlating the transverse spatial and longitudinal momentum distributions of quarks and gluons inside the proton, leading to a sum rule for the separate contributions of quarks and gluons to the spin of the proton [1].

The ep scattering kinematics in the Bjorken limit define a preferred longitudinal axis (up to ambiguities of order t/Q^2). Light cone momenta $P^\pm = (P^0 \pm P^z)/\sqrt{2}$ and light cone helicities of the external particles are defined with respect to this axis. The variables $x \pm \xi$ are the light cone momentum fractions of the initial and final active quark. The variable ξ is kinematic: $\xi \approx x_B/(2 - x_B)$, whereas x is integrated from -1 to 1 as a consequence of the implied quark loop. The experimental $ep \to ep\gamma$ scattering amplitude is the coherent sum of the Compton amplitude and the Bethe-Heitler (BH) amplitude, wherein the real photon is emitted by the incoming or the scattered electron, as illustrated in Fig. 1.

In this analysis of the Jefferson Lab Hall A experiment E12-06-114, we follow the Braun-Manashov-Müller-Pirnay (BMMP) formalism [6], wherein the longitudinal axis is defined in an event-by-event frame in which the three vectors $\mathbf{q}$ and $\mathbf{q}'$ are colinear. More generally, the light cone is defined by null vectors q' and $q - q'/(1 - t/Q^2)$. In this reference frame, the leading four Compton amplitudes conserve the light cone helicity of the photons. The proton helicity dependence of the Compton amplitude is expressed through the definition of four chiral-even Compton form factors (CFFs) ($\mathcal{H}_{++}$, $\tilde{\mathcal{H}}_{++}$, $\mathcal{E}_{++}$, $\tilde{\mathcal{E}}_{++}$), which are convolution integrals of the four corresponding GPDs. Each CFF is associated with a unique nucleon-spinor matrix element of, e.g., $\gamma^+, \gamma^+\gamma_5, \ldots$.

The reduction of the twelve Compton amplitudes to just four amplitudes, as first described in [3] is a profound simplification. Nonetheless in the range of Q^2 and x_B currently accessible, the remaining eight chiral-odd photon helicity-flip Compton amplitudes, while small, cannot be completely neglected.

The HERMES Collaboration performed extensive measurements of single- and double-spin DVCS asymmetries [7–9]. The H1 [10] and ZEUS [11] Collaborations measured the DVCS cross section over a broad range of Q^2 and W^2 at low x_B. The Jefferson Lab CLAS Collaboration has measured DVCS beam spin asymmetries and cross sections [12–14] and longitudinally polarized target asymmetries [15–17]. Recent experimental studies on DVCS show that the contributions of the chiral-even GPDs dominate the DVCS amplitude already at Q^2 values as low as 1.5 GeV^2 [13,18,19]. However, dynamic terms involving a photon helicity flip are not negligible, even though they are nominally suppressed by powers of $(t, M^2)/Q^2$ [20].

This Letter reports the results of experiment E12-06-114, which ran in Hall A at Jefferson Lab in the fall of 2014 and in 2016. Concurrent data on $ep \to ep\pi^0$ were published in [21], which also includes additional experimental and analysis details. Table I shows the nine kinematic settings in Q^2 and x_B at which the DVCS cross sections were measured. For each setting, the data are binned in t and the azimuth ϕ of the detected photon q' around the direction of $\mathbf{q}$, as defined by the "Trento convention" [22].

The longitudinally polarized electron beam impinged on a 15-cm liquid hydrogen target. The beam current was adjusted between 5 and 15 μA, depending on the kinematic setting, in order to maintain dead time below 5%. The Hall A Møller polarimeter measured an averaged beam polarization of $86 \pm 1\%$. The $H(\vec{e}, e'\gamma)X$ reaction was the main trigger of the data acquisition system. The scattered electron was detected by a coincidence signal between the scintillators and the Cerenkov detector of the left high-resolution spectrometer (HRS) [23]. The electron identification was further refined off-line by the use of a Pb-glass calorimeter in the HRS. The outgoing photon was detected by a dedicated highly segmented PbF$_2$ electromagnetic calorimeter. The analog signal from each of the 208 calorimeter channels was recorded over 128 ns by 1 GHz digitizing electronics based on the analog ring sampler (ARS) chip [24,25]. Following an HRS electron trigger (level 1), calorimeter signal sampling was stopped. Waveform digitization was validated by a level-2 trigger

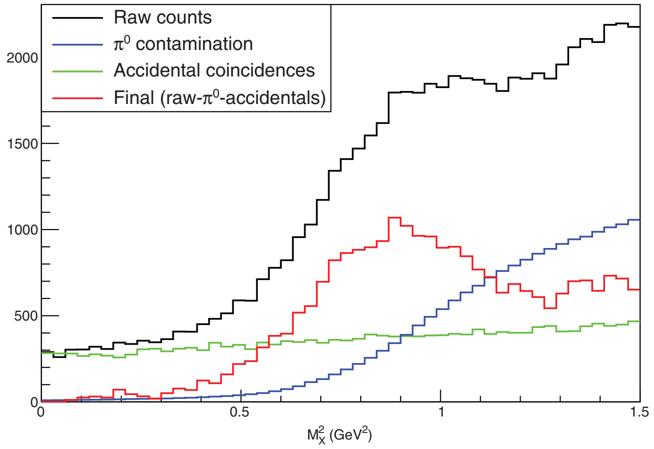

FIG. 2. Missing mass squared of the $ep \rightarrow e\gamma X$ reaction for kinematic setting Kin-48-1, integrated over t and ϕ. Experimental data are shown in black. The subtraction of the accidental contribution (green) and photons from π^0 decays (blue) yields the red histogram.

which computed the sum of the signal from all channels in a 80 ns window. If a signal above a programmable threshold was found in the calorimeter, the digitization process took 128 μs; otherwise the ARS system resumed sampling after 500 ns. The level-2 trigger was based on a field-programmable gate array module, and was used only during high counting rate settings (> 1 kHz). For settings with low rates, all level-1 triggers were validated and waveforms digitized [21]. Off-line analysis of the calorimeter signals and regular energy calibrations resulted in an energy resolution of 3% at 7 GeV. Missing-mass reconstruction identified the nondetected proton (see Fig. 2). The time resolution between the electron and photon detections was better than 1 ns. The number of random coincidences was evaluated by analyzing events in a time window shifted with respect to the coincidence time of the HRS and calorimeter signals.

An important source of background was neutral-pion electroproduction events for which only one of the decay photons was detected. The number of one-photon events from π^0 decays was estimated by a Monte Carlo simulation normalized bin by bin to the number of detected $\pi^0 \rightarrow \gamma\gamma$ events. The acceptance and resolution of the experiment were modeled by a GEANT4 simulation. The simulation included bin migration effects due to real and virtual radiation and the PbF_2 calorimeter energy resolution, as described in [19]. During the data taking, the first quadrupole of the HRS experienced the gradual failure of its cryogenic current lead. For the first part of the experiment, the faulty quadrupole could only be used at a reduced current supply. Before the fall 2016 data taking, that quadrupole was replaced by a room-temperature quadrupole providing a similar magnetic field. Optics calibrations data were taken to maintain the excellent resolution of the HRS. Effects on the spectrometer acceptance were taken into account for each kinematic setting and run period by

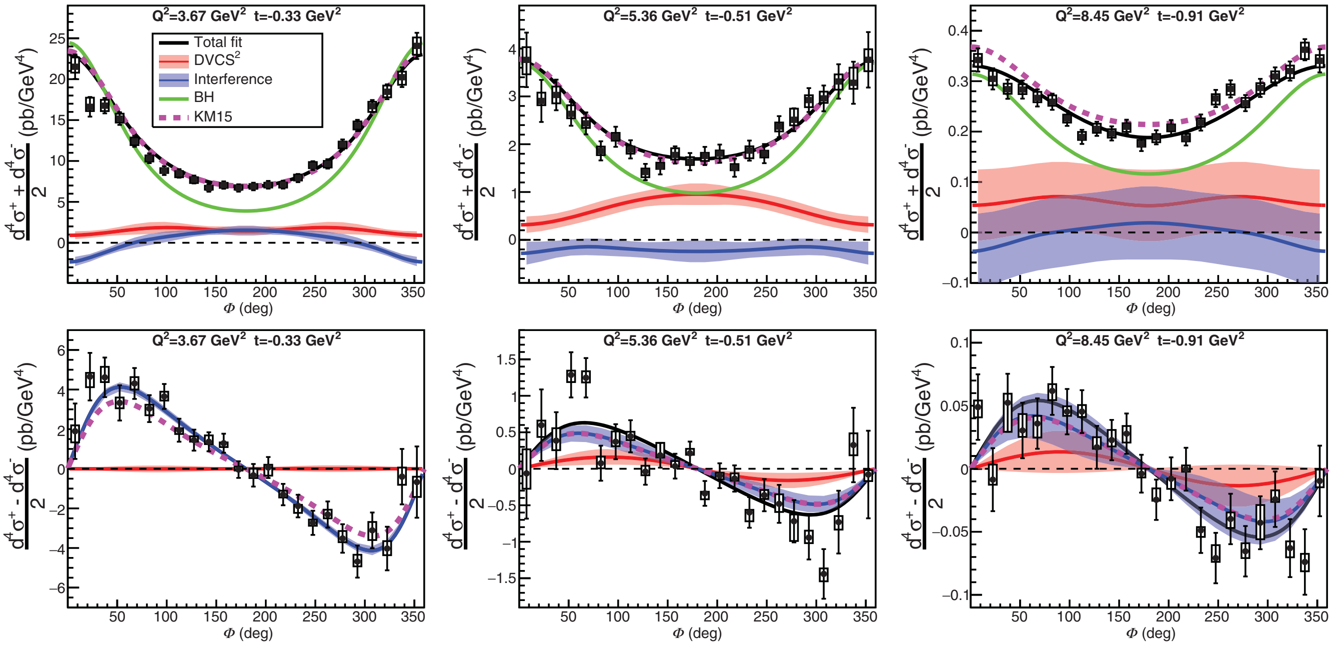

FIG. 3. Helicity-independent (top) and helicity-dependent (bottom) DVCS cross section at $x_B = 0.36$ (left), $x_B = 0.48$ (center), and $x_B = 0.60$ (right) for the values of Q^2 and t indicated on the top of each figure. Bars around the points indicate statistical uncertainty and boxes show the total systematic uncertainty, computed as the quadratic sum of the point-to-point and correlated systematic uncertainties. Black curves display the total fit to the cross sections, at constant x_B and t, in the BMMP formalism. The BH cross section is shown in green. The contribution from the BH-DVCS interference is shown by the blue bands, whereas the contribution from the DVCS^2 term is indicated by the red bands. All band widths correspond to one standard deviation. The KM15 model is shown in magenta.

applying similar multidimensional cuts (R cuts, [26]) on both the experimental and simulated data.

Deep inelastic scattering data were taken simultaneously to the main DVCS data using an ancillary trigger for all kinematic settings, which allowed a monitor of the scattered electron detection efficiency and acceptance [21]. The total systematic uncertainty of the DVCS cross-section measurements includes the uncertainty on the electron detection and acceptance, the luminosity evaluation, the uncertainty on the photon detection, and the exclusivity. Radiative corrections are included in the analysis based on calculations of [27] and using the procedure described in detail in [21].

Figure 3 shows a sample of the cross section measured at each of the x_B settings. See Supplemental Material [28] for the full set of data. The azimuthal dependence of the cross section is fit using the BMMP formalism [6], and the contribution from the BH-DVCS interference and DVCS^2 contributions are shown along with the BH cross section. The BMMP calculation includes kinematic power corrections $\sim t/Q^2$ and $\sim M^2/Q^2$ that were proven to be important at these kinematics [20]. The cross section is expressed as a function of helicity-conserving CFFs ($\mathcal{H}_{++}$, $\tilde{\mathcal{H}}_{++}$, $\mathcal{E}_{++}$, and $\tilde{\mathcal{E}}_{++}$), longitudinal-to-transverse helicity-flip CFFs ($\mathcal{H}_{0+}$, $\tilde{\mathcal{H}}_{0+}$, $\mathcal{E}_{0+}$, and $\tilde{\mathcal{E}}_{0+}$), and transverse helicity-flip CFFs ($\mathcal{H}_{-+}$, $\tilde{\mathcal{H}}_{-+}$, $\mathcal{E}_{-+}$, and $\tilde{\mathcal{E}}_{-+}$). For each GPD label, the subscripts λ, λ' refer to the light cone helicity of the initial (virtual) and final (real) photon, respectively. In this formalism, the light cone is defined by linear combinations of q^μ and q'^μ. Our whole dataset has been fitted using this complete and consistent scheme, with the real and imaginary part of all these CFFs being the free parameters (a total of 24) of the fit. All kinematics bins in Q^2 and ϕ at constant (x_B, t) are fitted simultaneously, however possible QCD evolution of the CFFs as functions of Q^2 is not considered.

While the number of fit parameters is large, the high accuracy of the data allows to simultaneously extract all the helicity-conserving CFFs with good statistical uncertainties. Figure 4 shows the real and imaginary part of all four helicity-conserving CFFs as a function of x_B averaged over t. These results represent the first complete extraction of all helicity-conserving CFFs appearing in the DVCS cross section, including the poorly known $\mathcal{E}_{++}$ and $\tilde{\mathcal{E}}_{++}$. The state-of-the-art GPD parametrization KM15 [29] that reproduces worldwide DVCS data show a reasonable agreement but fail to describe $\mathcal{E}_{++}$ and $\tilde{\mathcal{E}}_{++}$ accurately.

As first demonstrated in [20] and described theoretically in [30], the measurement of the DVCS cross section at two or more values of the ep center-of-mass energy $\sqrt{s}$ provides statistically significant separation of the real and imaginary parts of the BH-DVCS interference term as well as the DVCS^2 contribution in the cross sections for polarized electrons. A new analysis [31] of all previous JLab DVCS data followed a similar procedure, and obtained flavor-separated Compton form factors, after inclusion of our recent neutron DVCS data [32]. In the present analysis, realistic error bands on the chiral-even CFFs are obtained by explicit inclusion of higher-order terms (e.g., $\mathcal{H}_{0+}$, $\mathcal{H}_{-+}$, etc.) in the cross section fit, with these terms primarily constrained by inclusion of higher Fourier terms in the azimuthal variable ϕ. Although the extracted values of the helicity-flip CFFs are largely statistically consistent with zero, the statistical correlations between all of the CFF values at fixed x_B are essential to obtaining realistic experimental uncertainties. Figure 5 illustrates for setting $x_B = 0.60$ the values of CFFs as a function of t obtained when the fit includes only the helicity-conserving CFFs (red points) and when both helicity-conserving and helicity-flip CFFs are included (black points). One can see that fitting only helicity-conserving CFFs significantly underestimates their uncertainties.

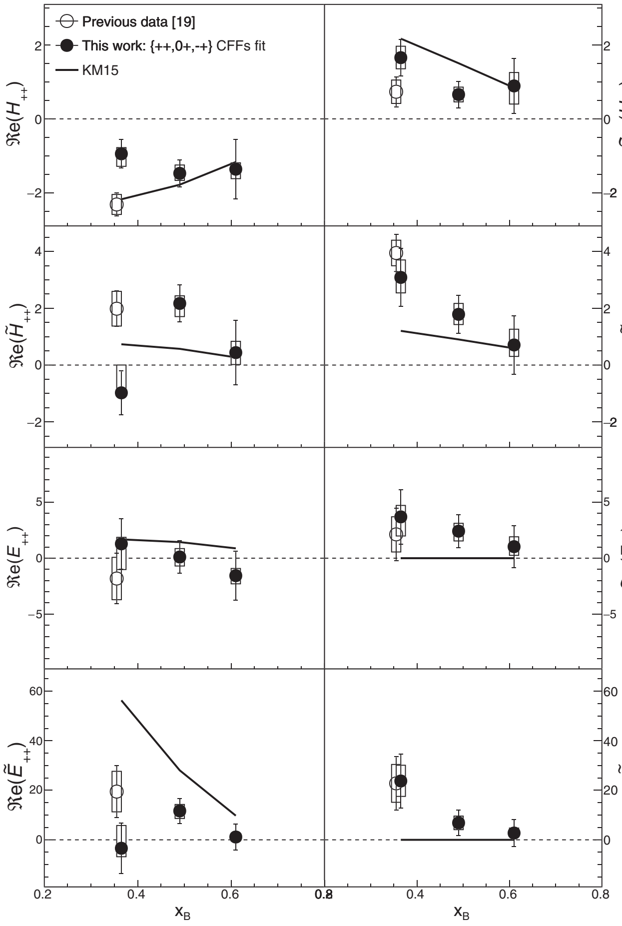

FIG. 4. Values of the helicity-conserving CFFs, averaged over t, as a function of x_B. Bars around the points indicate statistical uncertainty and boxes show the total systematic uncertainty. The fit results of previous data [19] at $x_B = 0.36$ are displayed with the open markers. The average t values are -0.281 GeV^2 [19] and -0.345, -0.702, -1.050 GeV^2 at $x_B = 0.36$, 0.48, 0.60, respectively. The solid lines show the KM15 model [29].

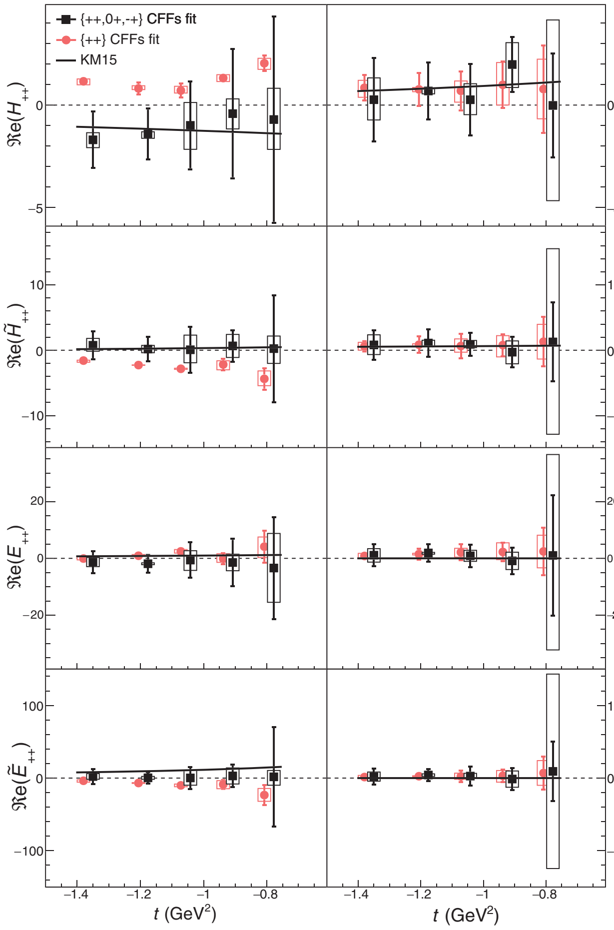

FIG. 5. Values of the helicity-conserving CFFs as a function of t at $x_B = 0.60$ obtained from a fit including only the helicity-conserving CFFs (red) and a fit including both helicity-conserving and helicity-flip CFFs (black). Red points are slightly offset for clarity. Bars around the points indicate statistical uncertainty and boxes show the total systematic uncertainty. The solid lines show the KM15 model [29].

The sensitivity to the CFFs $\mathcal{E}$ and $\tilde{\mathcal{E}}$ illustrated in Fig. 4 arises from the Q^2-dependent kinematic factors weighting these terms relative to the contributions of $\mathcal{H}$ and $\tilde{\mathcal{H}}$. The KM15 model [29] includes only the D term (support limited to $|x| < \xi$) in the E GPD, and therefore vanishes at $x = \xi$, resulting in $\mathcal{I}\mathrm{m}[\mathcal{E}] = 0$. For $\tilde{E}$, this model includes only the pion pole, via the $\gamma^*\gamma \to \pi^0$ amplitude, and thus the amplitude in this channel is also purely real. In contrast, the model of [33] for E includes a valence quark contribution with support outside the $|x| < \xi$ bound and therefore produces a nonzero imaginary part of the $\mathcal{E}$ CFF. Similarly, the chiral quark soliton model [33,34] produces a contribution to $\tilde{E}$ that while smaller in magnitude to the pion pole, is additive with opposite sign. This may explain the significant difference between our values of $\mathcal{R}\mathrm{e}[\tilde{\mathcal{E}}]$ and the KM15 model. GPDs can be described as momentum decompositions of the corresponding form factors. This is explicit in the first moment sum rules, which relate, e.g., GPDs E and $\tilde{E}$ (summed over quark flavor f) to the axial and pseudoscalar form factors G_A and G_P of the proton:

$$\sum_f \int_{-1}^{1} \left\{ \begin{matrix} E_f(x,\xi,t) \\ \tilde{E}_f(x,\xi,t) \end{matrix} \right\} dx = \left\{ \begin{matrix} G_A(-t) \\ G_P(-t) \end{matrix} \right\}. \qquad (1)$$

These form factors, particularly G_P, are much less well known experimentally than the usual electromagnetic form factors $G_{E,M}$. The present measurements of the CFFs $\mathcal{E}$ and $\tilde{\mathcal{E}}$ therefore provide constraints on the quark momentum distribution support of the corresponding form factors within this x_B range.

The present measurements will be complemented in this same general kinematic range in the near future by measurements in JLab Halls B and C, and longitudinally polarized proton measurements and neutron DVCS measurements in JLab Hall B. These measurements therefore demonstrate that the full extraction of experimental Compton form factors is within reach.

We acknowledge essential contributions by the Hall A collaboration and Accelerator and Physics Division staff at Jefferson Lab. This material is based upon work supported by the U.S. Department of Energy, Office of Science, Office of Nuclear Physics under Contract No. DE-AC05-06OR23177. This work was also supported by a DOE Early Career Award to S. C. D. for the development of the high power hydrogen target cells, the National Science Foundation (NSF), the European Union Horizon 2020 research and innovation program under Grant Agreement No 824093, the French CNRS/IN2P3, ANR, and P2IO Laboratory of Excellence, and the Natural Sciences and Engineering Research Council of Canada (NSERC).

---

[*] carlos.munoz@ijclab.in2p3.fr

[1] X. Ji, Phys. Rev. Lett. **78**, 610 (1997).
[2] J. C. Collins, L. Frankfurt, and M. Strikman, Phys. Rev. D **56**, 2982 (1997).
[3] X. Ji and J. Osborne, Phys. Rev. D **58**, 094018 (1998).
[4] D. Müller, D. Robaschik, B. Geyer, F. M. Dittes, and J. Horejsi, Fortschr. Phys. **42**, 101 (1994).
[5] I. I. Balitsky and A. V. Radyushkin, Phys. Lett. B **413**, 114 (1997).
[6] V. M. Braun, A. N. Manashov, D. Müller, and B. M. Pirnay, Phys. Rev. D **89**, 074022 (2014).
[7] A. Airapetian *et al.* (HERMES Collaboration), J. High Energy Phys. 10 (2012) 042.
[8] A. Airapetian *et al.* (HERMES Collaboration), J. High Energy Phys. 06 (2010) 019.
[9] A. Airapetian *et al.* (HERMES Collaboration), Phys. Lett. B **704**, 15 (2011).
[10] F. D. Aaron *et al.* (H1 Collaboration), Phys. Lett. B **659**, 796 (2008).

[11] S. Chekanov *et al.* (ZEUS Collaboration), J. High Energy Phys. 05 (2009) 108.

[12] F. Girod *et al.* (CLAS Collaboration), Phys. Rev. Lett. **100**, 162002 (2008).

[13] H. S. Jo *et al.* (CLAS Collaboration), Phys. Rev. Lett. **115**, 212003 (2015).

[14] N. Hirlinger Saylor *et al.* (CLAS Collaboration), Phys. Rev. C **98**, 045203 (2018).

[15] S. Chen *et al.* (CLAS Collaboration), Phys. Rev. Lett. **97**, 072002 (2006).

[16] E. Seder *et al.* (CLAS Collaboration), Phys. Rev. Lett. **114**, 032001 (2015); **114**, 089901(A) (2015).

[17] S. Pisano *et al.* (CLAS Collaboration), Phys. Rev. D **91**, 052014 (2015).

[18] C. Muñoz Camacho *et al.* (Jefferson Lab Hall A Collaboration, Hall A DVCS Collaboration), Phys. Rev. Lett. **97**, 262002 (2006).

[19] M. Defurne *et al.* (Jefferson Lab Hall A Collaboration), Phys. Rev. C **92**, 055202 (2015).

[20] M. Defurne *et al.*, Nat. Commun. **8**, 1408 (2017).

[21] M. Dlamini *et al.* (Jefferson Lab Hall A Collaboration), Phys. Rev. Lett. **127**, 152301 (2021).

[22] A. Bacchetta, U. D'Alesio, M. Diehl, and C. A. Miller, Phys. Rev. D **70**, 117504 (2004).

[23] J. Alcorn *et al.*, Nucl. Instrum. Methods Phys. Res., Sect. A **522**, 294 (2004).

[24] F. Feinstein (ANTARES Collaboration), Nucl. Instrum. Methods Phys. Res., Sect. A **504**, 258 (2003).

[25] F. Druillole, D. Lachartre, F. Feinstein, E. Delagnes, H. Lafoux, C. Hadamache, and J. Fopma (ANTARES Collaboration), IEEE Trans. Nucl. Sci. **49**, 1122 (2002).

[26] M. Rvachev, Effective use of Hall A Spectrometers with *R*-functions, Hall A Technical Note Jlab-TN-01-055, Jefferson Lab, 2001.

[27] M. Vanderhaeghen, J. M. Friedrich, D. Lhuillier, D. Marchand, L. Van Hoorebeke, and J. Van de Wiele, Phys. Rev. C **62**, 025501 (2000).

[28] See Supplemental Material at http://link.aps.org/supplemental/10.1103/PhysRevLett.128.252002 for the full set of cross-section measurements.

[29] K. Kumerički and D. Müller, EPJ Web Conf. **112**, 01012 (2016).

[30] B. Kriesten, A. Meyer, S. Liuti, L. C. Diaz, D. Keller, G. R. Goldstein, and J. O. Gonzalez-Hernandez, Phys. Rev. D **101**, 054021 (2020).

[31] M. Čuić, K. Kumerički, and A. Schäfer, Phys. Rev. Lett. **125**, 232005 (2020).

[32] M. Benali *et al.*, Nat. Phys. **16**, 191 (2020).

[33] K. Goeke, M. V. Polyakov, and M. Vanderhaeghen, Prog. Part. Nucl. Phys. **47**, 401 (2001).

[34] M. Penttinen, M. V. Polyakov, and K. Goeke, Phys. Rev. D **62**, 014024 (2000).